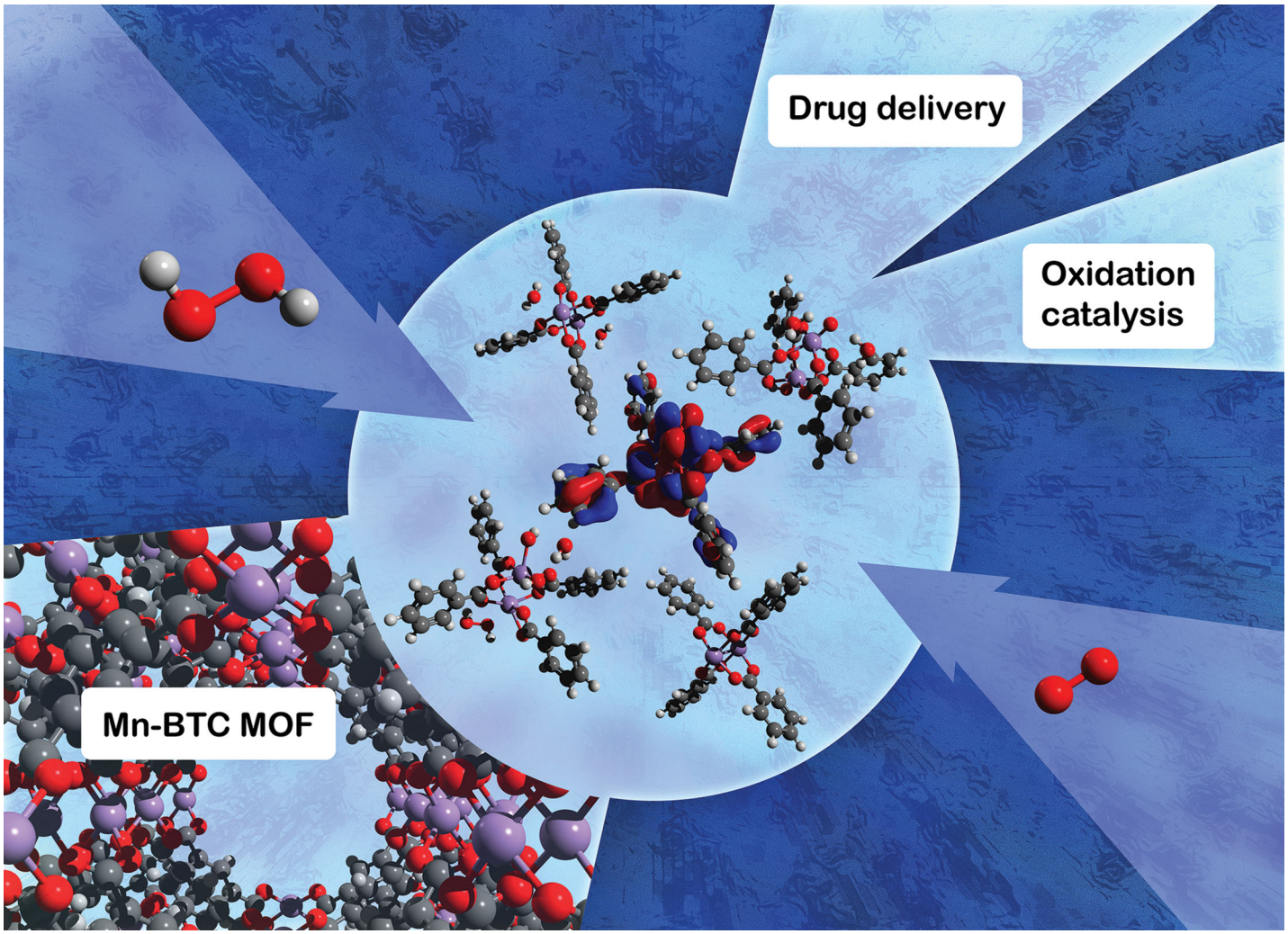

Showcasing research from the TheoMAT group of Prof. Dr Evgeny Pidko at ITMO University, Russia.

Degradation paths of manganese-based MOF materials in a model oxidative environment: a computational study

In this study, we modeled the oxidation mechanisms of an Mn-carboxylate MOF. DFT calculations showed the stability of Mn-BTC building blocks in an aqueous environment while the oxidative conditions promoted Mn-BTC decomposition. While the interaction with H_2O_2 species is of a non-covalent nature and required O–O-bond breaking to initiate Mn-center oxidation, open-shell O_2 species readily oxidized radical Mn-centers and formed bonds of σ-, π-, or δ-symmetry with the metal centers. The research provides an understanding of Mn-MOF-based system stability which is a crucial property in catalytic or targeted drug delivery applications.

As featured in:

See Mikhail V. Polynski, Evgeny A. Pidko *et al.*, *Phys. Chem. Chem. Phys.*, 2018, **20**, 20785.

ROYAL SOCIETY OF CHEMISTRY

rsc.li/pccp

Registered charity number: 207890

PCCP

PAPER

View Article Online
View Journal | View Issue

Cite this: *Phys. Chem. Chem. Phys.*, 2018, **20**, 20785

Degradation paths of manganese-based MOF materials in a model oxidative environment: a computational study†

Elena V. Khramenkova,[a] Mikhail V. Polynski,*[a] Alexander V. Vinogradov[a] and Evgeny A. Pidko *[ab]

Received 18th January 2018,
Accepted 26th April 2018

DOI: 10.1039/c8cp00397a

rsc.li/pccp

Stability is the key property of functional materials. In this work we investigate computationally the degradative potential of a model Mn-BTC (BTC = benzene-1,3,5-tricarboxylate) metal–organic framework (MOF) building block in aqueous solutions under oxidative conditions. Model density functional theory calculations have shown that the direct hydrolysis of the Mn-containing moieties is more difficult than their decomposition *via* oxidation-induced paths. While the interaction with H_2O_2 species is of non-covalent nature and requires O–O-bond breaking to initiate Mn-center oxidation, open-shell O_2 species readily oxidize radical Mn-centers and form bonds of σ-, π-, or δ-symmetry with the metal. The oxidative transformations of di-Mn paddle-wheel carboxylate structure-forming units are accompanied with substantial distortions of the coordination polyhedra that, together with the increased Lewis acidity of the oxidized metal centers, facilitates the hydrolysis leading to the degradation of the structure at a larger scale. Whereas such a mechanism is expected to hamper the catalytic applications of such Mn-MOFs, the associated structural response to oxidizing and radical species can create a basis for the construction of Mn-MOF-based drug delivery systems with increased bio-compatibility.

1. Introduction

Metal–organic frameworks (MOFs) are crystalline nanoporous structures, which consist of metallic coordination centers and organic ligands.[1,2] The key features of these materials are high crystallinity and well-defined highly porous structure along with unprecedented structural and functional tunability.[3,4] MOF-based materials and devices show great promise for various applications, ranging from gas sorption[5] and separation of enantiomers[6] to photonics[7] and catalysis.[8,9] Long-term stability and the ability to preserve the well-defined structure of the framework under operating conditions are the necessary features in the large-scale implementation of MOF-based systems and the lack of these may hamper their wide application.[10–12]

Fundamentally different requirements to material properties arise for biomedical applications. There is a growing interest in the utilization of inorganic chemistry polymers, including MOFs, in the development of multifunctional biomedical materials.[13,14] Here, the intrinsic instability of the hybrid organic–inorganic framework can be regarded as an advantageous feature enabling programmed degradation of the material.[15,16] The possibility of the programmed decomposition of an inorganic matrix into molecular building blocks[17,18] facilitates its removal from the organism as well as driving the controlled and targeted release of bio-active materials.[19,20] Therefore, MOFs are considered promising for the construction of responsive matrices and carriers for smart drug delivery systems.[21,22] Their predictable and tunable chemistry on the molecular level creates a possibility to design chemical response mechanisms to varying environmental conditions, *i.e.*,[23] one can design these materials to respond to specific changes in the microenvironment of pathological tissues. Acidosis, elevated tissue temperature, and formation of reactive oxygen species (ROS) are the specific signals that can direct the targeted delivery of an active pharmaceutical ingredient (API) to a pathologic area.[24–26] MOFs readily satisfy the essential requirements for smart drug delivery platforms, which are controllable degradation, biocompatibility and simplicity of chemical functionalization. They may be synthesized from biocompatible components as non-toxic metals and organic ligands. The medical use of widely explored Fe- and Cr-based MOFs is limited due to the toxicity issues, although such MOFs are able to upload high amounts of API.[27] In this context, Mn-based inorganic systems are particularly appealing owing

[a] *TheoMAT group, International Laboratory "Solution Chemistry of Advanced Materials and Technologies", ITMO University, Lomonosova str. 9, St. Petersburg 191002, Russia. E-mail: polynskimikhail@gmail.com*
[b] *Inorganic Systems Engineering group, Department of Chemical Engineering, Faculty of Applied Sciences, Delft University of Technology, Van der Maasweg 9, 2629 HZ Delft, The Netherlands. E-mail: E.A.Pidko@tudelft.nl*

† Electronic supplementary information (ESI) available. See DOI: 10.1039/c8cp00397a

to their low toxicity combined with Mn-rich coordination chemistry. While being toxic only at a high dosage,[28] Mn regulates biological processes and is a component of many enzymes.[29–31]

Mn-Based MOFs are also considered as catalysts for a number of important chemical processes. In particular, such Mn-MOFs as $[Mn_3(atpa)_3(dmf)_2]$ and $[Mn_2(tpa)_2(dmf)_2]$ were investigated as effective Lewis acid catalysts for the cyanosilylation of acetaldehyde (atpa = 2-aminoterephthalate, tpa = terephthalate, dmf = dimethylformamide).[32] The oxidative degradation of phenol catalyzed by bimetallic Fe/Mn-MOF-71 was studied by Sun *et al.*[33] According to Pereira *et al.*,[34] Mn-based PIZA, RPM and ZJU MOF families are catalytically active for alkane oxidation.

The behavior of Mn-based MOFs in oxidative environments has been a subject of several experimental studies. Depending on the nature of the ligands and the MOF structure, the intrinsic structural stability under harsh reaction conditions may vary substantially.[35–37] Zuluaga *et al.* have reported Mn-MOF-74's (Mn_2(DOBDC), DOBDC = 2,5-dioxido-1,4-benzenedicarboxylic acid) susceptibility to hydrolysis that led to the degradation of the structure and limited the sorption capacity of the material.[38] On the other hand, the report by Wu *et al.* demonstrated the perfect structural stability of a defected Mn-MOF-74 when exposed to water for up to 7 days.[39] The same framework material has been further employed for the catalytic oxidation of alkyl aromatics in an O_2 flow.[40] Hansen *et al.* reported an Mn-based catalyst featuring 2,2′:6′,2″-terpyridine structure-forming ligands as an active oxidation catalyst capable of retaining structural integrity in the catalytic oxidative environment.[41] MOF structures featuring Mn(3+)-porphyrin catalytic motifs have been reported as active and highly durable olefin oxidation catalysts.[42] An alternative IRMOF-3(Mn) catalyst made of Mn-carboxylate units was also found to be stable under the conditions of the gas-phase selective oxidation of alkenes.[43] Importantly, a wide range of catalytic studies have explored the reactivity of MOFs in non-aqueous media.[42–46] In biological systems, the aqueous environment may potentially make either direct or oxidation-induced hydrolysis possible as the routes for controlled decomposition of Mn-MOF. The stability of materials in oxidative environments has been the subject of computational studies as well.[47–49]

The interaction of MOF-based materials with the oxidizing species is thus of key importance for pharmaceutical chemistry and catalysis. The knowledge of the corresponding mechanisms on the molecular level may help to determine whether, on the one hand, a MOF material under consideration will irreversibly interact and (controllably) degrade under oxidative conditions. The understanding of controllable degradation mechanisms will allow for the construction of new targeted drug delivery systems. On the other hand, the material may be stable towards oxidizing species, reacting reversibly and activating them. Therefore, the understanding of the MOF-oxidizing species' interaction mechanism may direct new oxidation catalyst development as well.

The focus of the present computational study is the reactivity of the Mn-BTC framework (BTC = benzene-1,3,5-tricarboxylate, Fig. 1a) towards oxidizing species (O_2 and H_2O_2) in aqueous media. We show that the oxidative transformations of the Mn centers in MOFs can potentially be employed as the driver for controlled degradation of Mn-MOF-based nanocontainers in response to increased levels of oxidants produced in pathologic tissues. We computationally evaluated the energetics of the reaction mechanisms corresponding to the MOF–O_2- and MOF–H_2O_2-interactions in aqueous media. The results provide guidance towards the further design of responsive structures for a wider range of applications, including smart drug delivery systems. Besides, the insights into the processes determining the structural (in)stability of Mn-BTC frameworks under oxidative conditions are crucial for their utilization in oxidation catalysis.

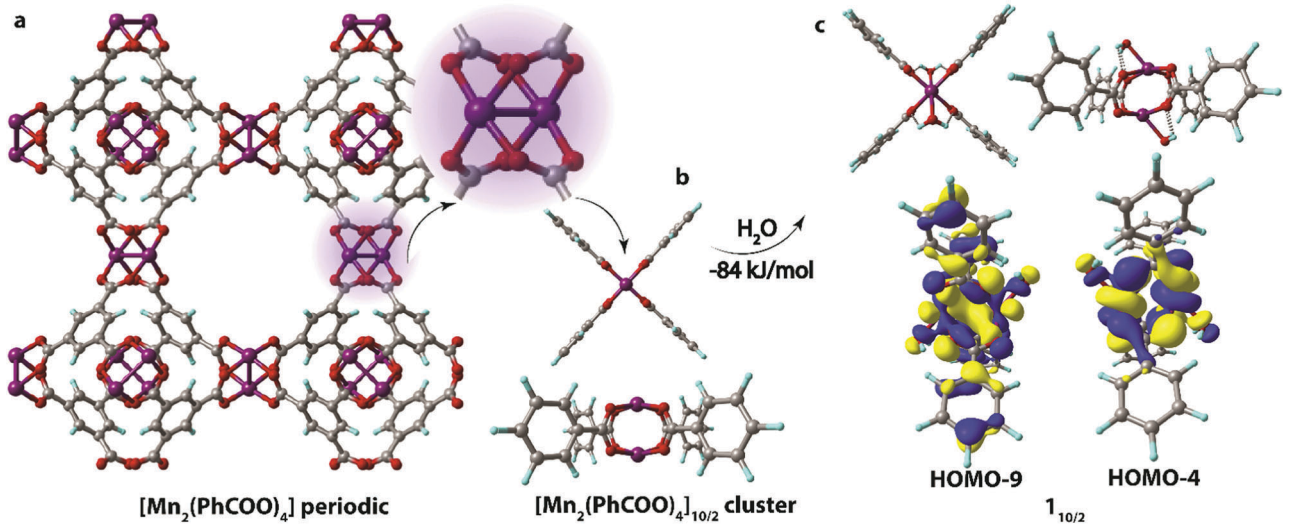

Fig. 1 The periodic structure of (a) Mn-BTC MOF and (b) the corresponding $[Mn_2(PhCOO)_4]$ cluster model in S = 10/2 spin state; (c) the $\mathbf{1_{10/2}}$ aqua complex along with the MOs representing the relevant molecular orbitals responsible for the Mn–H_2O binding (isosurface thresholds are 0.012 and 0.018 for HOMO−4 and HOMO−9 respectively). (b) and (c) optimized at the PBE-D3/6-31G(d,p) level of theory. Oxygen atoms are red, manganese atoms are purple, carbon atoms are grey, and hydrogen atoms are blue.

2. Computational methods

Density functional theory (DFT) calculations were performed using the Gaussian 09 D.01[50] program suite to study the structural properties of Mn-BTC MOF and elucidate its stability towards the oxidizing species (O_2 and H_2O_2) in water. Similar to our previous work on an MOF-based drug delivery system,[51] all calculations were carried out at the PBE-D3/6-311++G(d,p)//PBE-D3/6-31G(d,p) level of theory.[52,53] Dispersion attraction was accounted for using the empirical correction scheme proposed by Grimme.[54] Bulk solvent effects (water) were accounted for with the PCM solvation model[55] applied to single point calculations at the PBE-D3/6-311++G(d,p) level while the short-range interaction of Mn centers in Mn-BTC with H_2O molecules were accounted for by the explicit inclusion of H_2O species in the model systems. Vibrational frequencies were calculated analytically to evaluate the nature of the optimization-obtained stationary points.

The interaction with O_2 and H_2O_2 molecules and local structural deformations that could initiate the material degradation processes were investigated in the cluster-continuum approach. The cluster model representing the Mn-carboxylate paddle-wheel configuration was cut from a periodic structure of Mn-BTC MOF (Fig. 1a). The resulting cluster fragment of $[Mn_2(PhCOO)_4]$ was then coordinatively saturated by the inclusion of two water molecules. The geometries of all cluster models were optimized without any geometry constraints to satisfactorily represent the substantial geometrical flexibility and relaxation potential of the coordination polymers.[56,57] The effect of possible steric inflexibility was tested by the set of constrained optimizations, in which the positions of the para-H atoms of the $PhCOO^-$ units were fixed. These constrained test optimizations were carried out on the configurations corresponding to the most stable (in terms of exothermicity of formation) and distorted complexes obtained through the unconstrained optimizations. The computed energetics and optimized structures are summarized in the Supporting Information for the article (Fig. S1, S2 and Table S1, ESI†). These tests evidence the key role of the structural flexibility for the preservation of the optimal coordination environment of the Mn centers. The excessive geometrical strain imposed by the fixed positions of the para-H-atoms in $PhCOO^-$ ligands gave rise to the decoordinaton of Mn-centers in some cases.

All $L[Mn_2(PhCOO)_4]L$ model complexes (where L is H_2O, H_2O_2, or O_2) were considered in various spin states (namely, S = 6/2, 8/2, 10/2) while in the case of $H_2O[Mn_2(PhCOO)_4]O_2$ and $O_2[Mn_2(PhCOO)_4]O_2$ complexes, S = 12/2 and 14/2 spin states were also considered. Initial test calculations indicated that the other electronic configurations (including the lower-spin and broken symmetry configurations, see below) are characterized by excessively high energies and are therefore not relevant to the processes considered here.

The concurrent adsorption energies (E_{ads}) of the oxidizing species were calculated according to the formula:

$$E_{ads} = En_{-OX\text{-}Mn\text{-}BTC} + nE_{H_2O} - E_{AQUA} - nE_{OX}$$

where $En_{-OX\text{-}Mn\text{-}BTC}$ is the total energy of the $L[Mn_2(PhCOO)_4]L$ complex, E_{AQUA} is the energy of the aqua complex further designated as $\mathbf{1_{10/2}}$ (Fig. 1c), E_{H_2O} and E_{OX} are, respectively, the total energies of H_2O and O_2 or H_2O_2 molecules, and n is the number of H_2O molecules substituted in the process.

The molecular orbital isosurfaces used for the analysis of bonding in the adsorption complexes were constructed with the ChemCraft program.[58]

3. Results and discussion

3.1. Starting configurations

The structure unit of the Mn-BTC metal–organic framework (Fig. 1a) was modeled as the $[Mn_2(PhCOO)_4]$ cluster (Fig. 1b). The structure of Mn-BTC is represented by a periodic array of dimeric Mn^{2+} paddle-wheel centers linked by four benzene-1,3,5-tricarboxylic ligands (BTC). A number of spin states are accessible to the dimeric $[Mn_2(PhCOO)_4]$ species since the carboxylate ligand are formally considered to be of weak-field class. Particularly, 6/2, 8/2, 10/2 spin configurations as well as the broken symmetry singlet state were considered. In the case of the $[Mn_2(PhCOO)_4]$ cluster, high-spin S = 10/2 state with the square-planar coordination of the Mn^{2+} cations having the paddle-wheel structure was the most energetically favorable. The lower spin-states of S = 6/2 and 8/2 were less favorable (by 10 and 19 kJ mol^{-1}), respectively. To ensure the unlikeliness of the singlet state with the antiferromagnetic coupling of the unpaired electrons in the two metal centers, broken symmetry calculations were performed. The configuration resulting from the computation at the PBE-D3/6-311++G(d,p)//PBE-D3/6-31G(d,p) level (PCM solvation included) had 238 kJ mol^{-1} higher electronic energy compared to the lowest-lying 10/2 state and the antiferromagnetic coupling was confirmed by the analysis of the Mulliken spin densities, which had values of 2.6 and −2.9 a.u. on the Mn centers.

In aqueous solution, the open axial coordination sites are likely to be occupied by H_2O molecules. Among the $H_2O[Mn_2(PhCOO)_4]H_2O$ complexes, the one with S = 10/2 spin state, the $\mathbf{1_{10/2}}$ complex (Fig. 1c), was energetically preferred, and the low-spin S = 8/2 ($\mathbf{1_{8/2}}$) and 6/2 ($\mathbf{1_{6/2}}$) states had higher energies (43 and 54 kJ mol^{-1}, respectively). Thereby, $\mathbf{1_{10/2}}$ formation from the $[Mn_2(PhCOO)_4]$ complex in the 10/2 spin state is exothermic by −84 kJ mol^{-1}. The formation of the antiferromagnetic state was unlikely in the case of the $H_2O[Mn_2(PhCOO)_4]H_2O$ complex as well since the broken-symmetry computation at the PBE-D3/6-311++G(d,p)//PBE-D3/6-31G(d,p) level (PCM solvation included) showed that the singlet state had 332 kJ mol^{-1} higher energy compared to the 10/2 state. The Mulliken spin densities in the Mn-centers in the singlet state were 4.5 and −4.5 a.u.

Water-bound cluster $\mathbf{1_{10/2}}$ (Scheme 1) was selected as the reference point and starting configuration for further modeling the interaction of Mn-BTC with the oxidizing species. It is worth noting that the overlap between H_2O and $[Mn_2(PhCOO)_4]$ fragments in $\mathbf{1_{10/2}}$ is negligible (Fig. 1c), although the binding is highly exothermic (ΔE_{ads} = −84 kJ mol^{-1}). The coordination of H_2O molecules results in the formation of the four hydrogen bonds between OH groups and the oxygen atoms of the carboxylate ligands. Thus, the highly exothermic effect of H_2O binding may

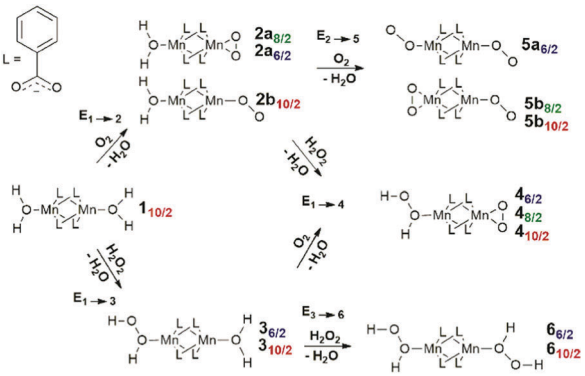

Scheme 1 A stepwise path for coordination of oxidizing species to $\mathbf{1_{10/2}}$ complex.

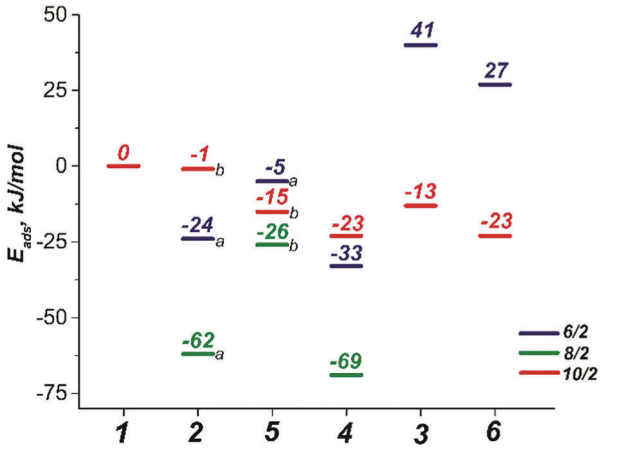

Fig. 2 The concurrent adsorption energies (E_{ads}, see Section 2) of the O_2 and H_2O_2 oxidizing species to $H_2O[Mn_2(PhCOO)_4]H_2O$ complex.

be caused by the formation of strong hydrogen bonds and the reduction of electrostatic repulsion between Mn^{2+} cations owing to the countering electrostatic field of H_2O dipoles.

Scheme 1 summarizes the chemical transformations that are considered here as potential pathways for the oxidative degradation of Mn-BTC in the presence of O_2 or H_2O_2 species. The model oxidants are relevant to both biological and catalytic potential applications of Mn- and carboxylate-based metal–organic frameworks. Note that, depending on the spin-state, coordination complexes of different structures are formed; Scheme 1 explicitly indicates them with the appropriate labels. Fig. 2 graphically summarizes the relative energies of the formation of the oxidated complexes. These oxidative transformations are discussed in more detail in the subsequent sections.

3.2. O_2 binding

The binding of an O_2 molecule to the coordinately unsaturated Mn centers in Mn-BTC (**1** → **2**, Scheme 1) may result in two isomeric structures that are in the end-on (η^1) and side-on (η^2) configurations. The end-on configuration is the result of the 2σ-type bonding of the O_2 molecule with the Mn^{2+} cation while the side-on configuration is the complex having δ-type bond that corresponds to the binding of both oxygen atoms to the Mn^{2+} center. It should be noted that metal–ligand δ-symmetry bonding is somewhat unusual since it is usually observed in transition metal complexes with quadruple metal–metal bonds.[59]

The binding in both coordination modes results from the overlap between singly-occupied O_2 π* orbitals and 3d orbitals of Mn that are singly occupied as well, and the formation of the particular configuration leads to different spin states. Whereas the formation of the η^1 complex preserves the spin state (with the corresponding structure being $\mathbf{2b_{10/2}}$, see Scheme 1), the formation of δ complexes with η^2-bound O_2 ligand leads to the electron pairing and the formation of $\mathbf{2a_{6/2}}$ and $\mathbf{2a_{8/2}}$ complexes in 6/2 and 8/2 spin states, respectively. The formation of the latter is strongly exothermic. The reaction energies computed for water exchange 1 → 2 are −24 and −62 kJ mol^{-1} for the formation of $\mathbf{2a_{6/2}}$ and $\mathbf{2a_{8/2}}$, respectively (Fig. 2). The formation of the σ-type bound $\mathbf{2b_{10/2}}$ complex in the 1 → 2 process has a weak exothermic effect of −1 kJ mol^{-1}. The chemical irrelevance of the high-spin 12/2 state was ensured with the computed binding energy of 42 kJ mol^{-1} (see Fig. S3a, ESI†).

The complexation with O_2 distorts the initial square pyramidal geometry of the Mn centers in $\mathbf{1_{10/2}}$ to form a distorted octahedron in $\mathbf{2a_{6/2}}$ and trigonal bipyramid in $\mathbf{2a_{8/2}}$ of O_2-coordinated Mn sites. The water-coordinated site in $\mathbf{2a_{6/2}}$ has octahedral geometry while the H_2O-bonded Mn^{2+} center in $\mathbf{2a_{8/2}}$ has severely distorted trigonal-bipyramidal geometry with the cleaved Mn–Mn bond. Mn centers in $\mathbf{2b_{10/2}}$ form highly distorted octahedrons (Fig. 3c).

The end-on-bound O_2 molecule in $\mathbf{2b_{10/2}}$ may formally be considered as a superoxide (O_2^-) ligand, which implies the formal oxidation of Mn(2+) to Mn(3+). The formal oxidation state of oxygen-bound Mn cations in $\mathbf{2a_{6/2}}$ and $\mathbf{2a_{8/2}}$ complexes should then be considered as Mn(4+) with the side-on bound peroxide (O_2^{2-}) ligands.

The changes in the Mn oxidation states are in line with the Mulliken spin density changes in reaction 1 → 2 (Scheme 1). The O_2 binding in the case of $\mathbf{2b_{10/2}}$ leads to the decrease of the spin density on the interacting Mn (from 4.80 to 3.56) and the asymmetric decrease from (1, 1) to (0.70, 0.82) of the spin densities on O atoms in the O_2 molecule (see Table S2, ESI†). Based on the analysis of the spatial distribution of Kohn–Sham orbitals, σ-symmetry bonding is evident when a single O atom is bound to Mn. This implies the formation of an Mn center in the formal (3+) oxidation state.

The δ binding of the O_2 species proceeded *via* the electron density donation by Mn d electrons to the π* orbitals of O_2 molecules resulting in the weakening of the O–O bond. This is reflected in the significant increase of the O–O bond length in $\mathbf{2a_{8/2}}$ and $\mathbf{2a_{6/2}}$ structures (r(O–O) = 1.411 Å and 1.373 Å, respectively) when compared to that in the dioxygen molecule (r(O–O) = 1.228 Å). The analysis of the electron density distribution in $\mathbf{2a_{6/2}}$ shows the decrease of spin density on oxygen atoms in the O_2 molecule (from (1, 1) to (0.15, 0.15) a.u.) and the reduction of spin density values on the corresponding Mn site (from 3.16 to 2.33). A similar trend was found in $\mathbf{2a_{8/2}}$ where spin densities on the Mn site and the coordinated O_2 decreased from 3.28 to 2.94 and from (1, 1) to (0.11, 0.10), respectively (see Table S2, ESI†). These changes indicate the formation of the Mn(4+) formal oxidation state in both cases.

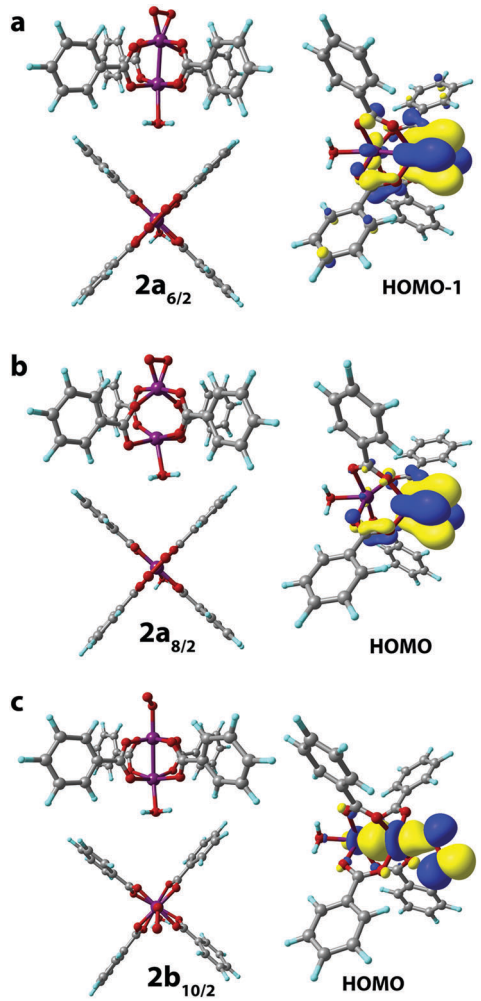

Fig. 3 Geometries were optimized at the PBE-D3/6-31G(d,p) level of theory (front and side views are given). The key bonding MOs of the $O_2[Mn_2(PhCOO)_4]H_2O$ complexes in S = 6/2 (a), 8/2 (b), and 10/2 (c) spin states are depicted with isosurface thresholds eq. 0.023.

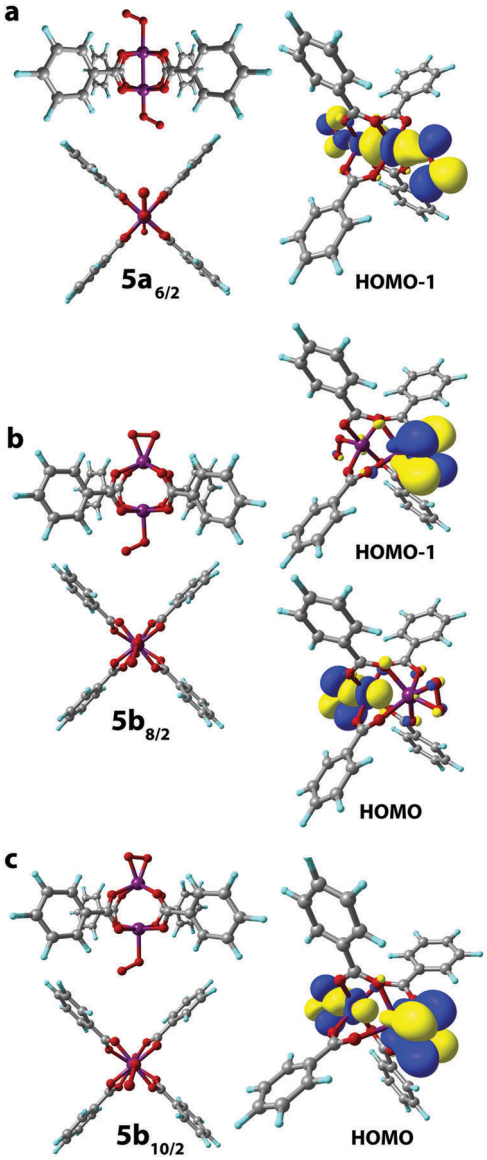

Fig. 4 Geometries were optimized at the PBE-D3/6-31G(d,p) level of theory (front and side views are given). The key bonding MOs of the $O_2[Mn_2(PhCOO)_4]O_2$ complexes in S = 6/2 (a), 8/2 (b), and 10/2 (c) spin states are depicted with isosurface thresholds eq. 0.023.

The reaction of **2a** and **2b** complexes with a second O_2 molecule leads to the formation of two isomers (end-on-end-on and side-on-end-on) of the three possible ones (**2** → **5** step on the Scheme 1). The formation of the side-on-side-on $O_2[Mn_2(PhCOO)_4]O_2$ isomer was not observed owing to the significant steric strain of the $[Mn_2(PhCOO)_4]$ core imposed by the side-on binding of O_2 species (see the discussion above and Fig. 3a–c).

The σ-type bonding of two oxygen molecules leads to an end-on-end-on configuration with the octahedral coordination of both Mn cations. The formation of the corresponding $\mathbf{5a_{6/2}}$ complex proceeded with a low exothermic effect of −5 kJ mol^{-1} (Fig. 4a). The side-on-end-on configuration corresponds to the simultaneous binding of O_2 species in δ- and σ-modes and the formation of $\mathbf{5b_{8/2}}$ and $\mathbf{5b_{10/2}}$ complexes is exothermic by −26 and −15 kJ mol^{-1}, respectively (Fig. 4b and c). Here, both Mn centers adopt square pyramidal geometry.

The Mn centers having an η^2-bound O_2 ligand in $\mathbf{5b_{8/2}}$ and $\mathbf{5b_{10/2}}$ isomers were in Mn(4+) oxidation state as follows from the significant alternation of the spin densities upon their formation that is the spin density on the O atoms of the ligand changes from (1, 1) to (−0.27, −0.27) and (0.15, 0.15), respectively. At the same time, the spin density at the η^1-bound O_2 ligand in $\mathbf{5b_{8/2}}$ and $\mathbf{5b_{10/2}}$ changed from (1, 1) to (0.38, 0.46) and (0.78, 0.93), respectively, suggesting the oxidation of the metal center to the Mn(3+) state (see Table S2, ESI†).

The $\mathbf{5_{14/2}}$ spin isomer corresponds to weak non-covalent bonding. Particularly, the lack of close Mn–O contacts is evident in the optimized structures (see Fig. S3b, ESI†) and the corresponding reaction energy is equal to 84 kJ mol^{-1}.

The Mn(3+) state is known to easily disproportionate leading to Mn(2+) and Mn(4+) formation in aqueous solutions.[60] Accordingly, our calculations show that the formation of η^1-bound O_2 complexes, which are the superoxide-bound (O_2^-)

Mn(3+) cations in $L[Mn_2(PhCOO)_4]L$, is the least exothermic reaction ($\mathbf{5a_{6/2}}$ and $\mathbf{2b_{10/2}}$ formation) among the alternative pathways. Therefore, we conclude that the oxidation of Mn-BTC MOF with O_2 forming Mn(3+) centers is less likely than the two-electron oxidation paths resulting in the oxidized structures with more stable Mn(4+) centers.

Compared to the exothermic step 1 → 2, in which the first O_2 molecule binds, the binding of the second O_2 molecule is strongly endothermic. The formation of $\mathbf{5a_{6/2}}$ and $\mathbf{5b_{8/2}}$ increases the energies of the systems by 19 and 36 kJ mol^{-1} compared to $\mathbf{2a_{6/2}}$ and $\mathbf{2a_{8/2}}$, respectively. Only formation of the σ-type bound complex $\mathbf{2b_{10/2}}$ is exothermic by −14 kJ mol^{-1}. The unfavorable binding of the second O_2 molecule in the cases of δ complexes is supposedly a result of the distorted and, consequently, more sterically strained structure of the oxidized species. The results above on the facile oxidation and substantial structural distortions of the coordination sphere of Mn centers upon O_2 coordination imply that the degradation of Mn-BTC MOFs can already be induced at low O_2 concentrations, thus creating an opportunity to develop O_2-selective response matrices as a basis for new smart drug delivery platforms.

3.3. H_2O_2 binding

Next, we computationally investigated the interaction of the Mn-BTC structure-forming unit $\mathbf{1_{10/2}}$ with H_2O_2 species. The binding results in the formation of two spin isomers (namely, $\mathbf{3_{6/2}}$ and $\mathbf{3_{10/2}}$) *via* the **1** → **3** process. The isomers have qualitatively close structures with the H_2O_2 molecule bound in end-on configuration. The formation of the low-spin complex with octahedral structure of Mn centers ($\mathbf{3_{6/2}}$, Fig. 5a) was highly endothermic with the reaction energy of 41 kJ mol^{-1}. The formation of the high-spin complex $\mathbf{3_{10/2}}$ was exothermic by −13 kJ mol^{-1} and the Mn center acquired a severely distorted trigonal-bipyramidal structure (Fig. 5b). The negligible change of the Mulliken spin density on the Mn centers (from 3.16 to 3.14) and (from 4.80 to 4.77) for $\mathbf{3_{6/2}}$ and $\mathbf{3_{10/2}}$, respectively, illustrates a purely non-covalent nature of H_2O_2 binding that does not directly induce the oxidation of the Mn centers (see Table S2, ESI†).

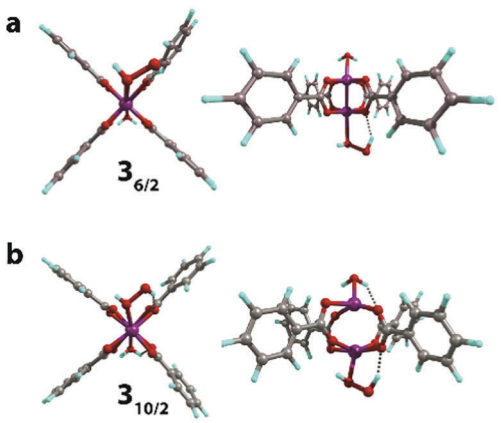

Fig. 5 The geometries (front and side views) of the $H_2O[Mn_2(PhCOO)_4]$-H_2O_2 complex in S = 6/2 (a) and 10/2 (b) spin states optimized at the PBE-D3/6-31G(d,p) level of theory.

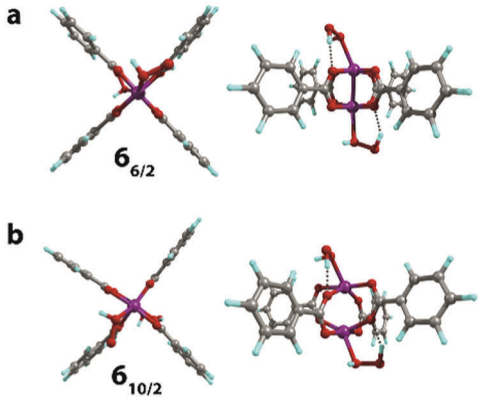

Fig. 6 The geometries (front and side views) of the $H_2O_2[Mn_2(PhCOO)_4]$-H_2O_2 complex in S = 6/2 (a) and 10/2 (b) spin states optimized at the PBE-D3/6-31G(d,p) level of theory.

The binding of the second H_2O_2 molecule *via* the **3** → **6** process proceeded with the retention of the coordination polyhedra and led to the formation of $\mathbf{6_{6/2}}$ and $\mathbf{6_{10/2}}$ (Fig. 6). These reactions had thermal effects of 27 and −23 kJ mol^{-1}, respectively.

The exchange of two water ligands with H_2O_2 leads to the coordination bond, which is accompanied by a negligible decrease of the Mulliken spin density on the Mn centers in both $\mathbf{1_{6/2}} \rightarrow \mathbf{6_{6/2}}$ and $\mathbf{1_{10/2}} \rightarrow \mathbf{6_{10/2}}$ transformations (from 3.16 to 3.14 and from 4.80 to 4.77, respectively; see Table S2, ESI†). These changes clearly show that the binding of H_2O_2 is not accompanied by the oxidation of the Mn centers. The final complexes in the **1** → **3** and **3** → **6** steps are stabilized *via* the formation of the five-membered cycles with the hydrogen bonds between oxygen atoms of the carboxylate ligands and the OH groups of the bound H_2O_2 species (r(OH···O) = 1.7–2.0 Å). In the case of $\mathbf{6_{6/2}}$ and $\mathbf{6_{10/2}}$, two H_2O_2 molecules bound to both Mn sites form two five-member cyclic structures contributing to their increased stability, resulting in the thermodynamic favorability of the ligand exchange.

3.4. Combined O_2 and H_2O_2 binding

Finally, we considered the possibility of the simultaneous binding of O_2 and H_2O_2 species *via* the **1** → **4** process. The geometry optimization procedures resulted in a structure of only one structural type to be formed having η^2-bound O_2 and weakly (covalently) bound H_2O_2 molecules. The O_2-coordinated Mn sites in all **4** complexes adopted a trigonal-bipyramidal configuration (Fig. 7). The high-spin $\mathbf{4_{10/2}}$ complex showed the highest degree of structural distortion upon formation. Notably, the formation of all three possible complexes $\mathbf{4_{6/2}}$, $\mathbf{4_{8/2}}$, and $\mathbf{4_{10/2}}$ was exothermic with reaction energies of −33 kJ mol^{-1}, −69 kJ mol^{-1} and −23 kJ mol^{-1}, respectively. The oxidation states of the Mn centers in the formed $H_2O_2[Mn_2(PhCOO)_4]O_2$ complexes are (2+, 4+), (2+, 4+), and (2+, 4+), respectively. The Kohn–Sham orbital and the Mulliken spin density analyses clearly illustrate the (2+, 4+) formal oxidation states in both $\mathbf{4_{6/2}}$ and $\mathbf{4_{8/2}}$ spin isomers. Spin density values on O atoms in the O_2 ligand are notably reduced from (1, 1) to (0.15, 0.15) and (0.11, 0.11) in $\mathbf{4_{6/2}}$ and $\mathbf{4_{8/2}}$, respectively (Table S2, ESI†). The spin density values on the

O_2-bound Mn site decreased upon formation of $\mathbf{4_{6/2}}$ (from 3.16 to 2.35) and $\mathbf{4_{8/2}}$ (from 3.28 to 2.91). Less pronounced spin density changes were observed in the $\mathbf{1_{10/2}} \rightarrow \mathbf{4_{10/2}}$ process. Particularly, the change from 4.80 to 3.88 a.u. was observed on the Mn cation. In the case of the O_2 ligand, the observed change was from (1, 1) to (0.42 to 0.61) a.u. (Table S2, ESI†). The key bonding orbital analysis (Fig. 7) corroborates the π-symmetry bonding and the formation of the Mn center in the (+4) formal oxidation state. The lower exothermicity of the formation of $\mathbf{4_{10/2}}$ compared to the $\mathbf{4_{6/2}}$ and $\mathbf{4_{8/2}}$ isomers is in line with the lower orbital overlap (no δ-symmetry bond formed).

3.5. Reactivity

Degradation of the MOF material in aqueous solutions may potentially occur either *via* the direct hydrolysis of the metal-carboxylate moieties or *via* the oxidation of the metal-containing nodes. Whereas our calculations suggest that the latter mechanism should dominate the structural response of Mn-BTC to the oxidative conditions in the presence of molecular O_2, the mechanism of MOF degradation in the presence of H_2O_2 as the oxidant requires the combination of the metal oxidation with a hydrolytic process. Indeed, no significant deformation of the $[Mn_2(PhCOO)_4]$ structural unit was observed upon H_2O_2 binding. The coordinatively unsaturated metal centers in the $[Mn_2(PhCOO)_4]$ cluster tend to bind strongly with the open-shell O_2 species owing to the radical nature of the former. The degradation of Mn-BTC *via* the oxidation by H_2O_2 closed-shell species may have a more complex mechanism. The adsorption complexes **6** discussed above thus become the starting point for the computational assessment of the feasibility of such a complex oxidation-assisted hydrolysis mechanism.

The oxidation-assisted hydrolysis thus starts with the substitution of the water molecules in the solvated $\mathbf{1_{10/2}}$ structure discussed in detail previously and the formed $\mathbf{6_{6/2}}$ and $\mathbf{6_{10/2}}$ intermediates undergo further oxidation (Fig. 6). The transition state on the potential energy surface with 10/2 spin state is denoted as $\mathbf{TS_{10/2}}$ and corresponds to a barrier of 21 kJ mol^{-1}. The computed imaginary frequency of the $\mathbf{TS_{10/2}}$ structure has the value of i365 cm^{-1}, corresponding to the O–O-bond stretching in the H_2O_2 moiety and the neighbouring Mn site has the trigonal-bipyramidal coordination polyhedron. After passing $\mathbf{TS_{10/2}}$, the relative order of the potential energy surfaces with S = 10/2 and 6/2 changes and the system may undergo a spin crossing.

For the high-spin complex $\mathbf{7_{10/2}}$, the O–O bond cleavage in the peroxide moiety leads to Mn(4+) center formation, which has octahedral geometry and bears two terminal OH ligands. The oxidation is accompanied with the reduction of the Mulliken spin density value in the Mn center (4.78 to 3.90 a.u.; Table S3, ESI†). The reaction energy for the latter process is −87 kJ mol^{-1}. The subsequent hydrolysis leads to H_2O binding to the Mn(4+) site through the formation of the hydrogen bonds between H atoms of H_2O molecule and O sites of the hydroxyl and benzoate ligands. The corresponding intermediate is denoted as $\mathbf{8_{10/2}}$ (Fig. 8). The non-valent H_2O molecule coordination does not alter the octahedral geometry of the Mn(4+) centers.

The Mn-BTC degradation *via* the 6/2 pathway was thermodynamically preferred according to the modeling results. The $\mathbf{7_{6/2}}$

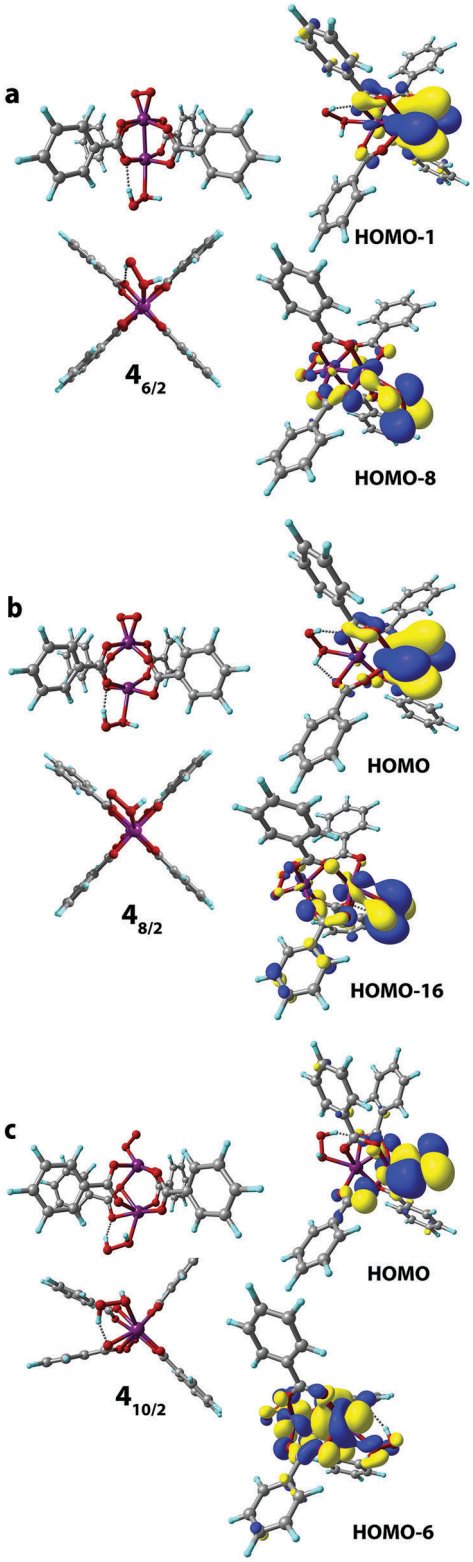

Fig. 7 Geometries were optimized at the PBE-D3/6-31G(d,p) level of theory (front and side views are given). The key bonding MOs of the $H_2O_2[Mn_2(PhCOO)_4]O_2$ complex in S = 6/2 (a), 8/2 (b), and 10/2 (c) spin states are depicted (isosurface thresholds are 0.023 (a), 0.023 for HOMO and 0.018 for HOMO−16 (b), and 0.023 for HOMO and 0.018 for HOMO−6 (c)).

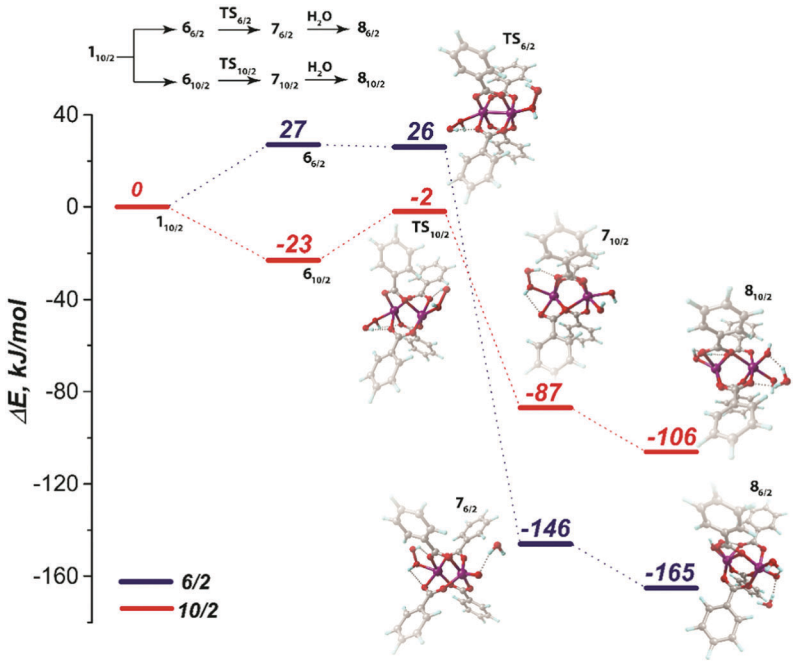

Fig. 8 Reaction energy profiles for the oxidation-induced hydrolysis of $\mathbf{6_{6/2}}$ and $\mathbf{6_{10/2}}$. The optimized structures of the initial ($\mathbf{6_{6/2}}$, $\mathbf{6_{10/2}}$), transition ($\mathbf{TS_{6/2}}$, $\mathbf{TS_{10/2}}$), final oxidized ($\mathbf{7_{6/2}}$, $\mathbf{7_{10/2}}$) and hydrolyzed states ($\mathbf{8_{6/2}}$, $\mathbf{8_{10/2}}$) are presented next to the corresponding energy levels. All geometries were optimized at the PBE-D3/6-31G(d,p) level of theory.

intermediate had −146 kJ mol^{-1} lower energy relative to the $\mathbf{1_{10/2}}$ level and −59 kJ mol^{-1} lower relative to the $\mathbf{7_{10/2}}$ counterpart. We expect the $\mathbf{6_{6/2}}$ to $\mathbf{7_{6/2}}$ transition to be barrierless. Particularly, the "barrier" of −1 kJ mol^{-1}, which was computed at the PBE-D3/6-311++G(d,p)//PBE-D3/6-31G(d,p) level with the PCM solvation model, could be an inaccuracy caused by the solvation model that was applied in post-optimization single-point energy refinement. The imaginary mode in the $\mathbf{TS_{6/2}}$ structure corresponded to O–O bond stretching and had the frequency of i261 cm^{-1} as computed at the PBE-D3/6-31G(d,p) level of theory. The oxidized Mn(4+) center in the $\mathbf{7_{6/2}}$ intermediate had a trigonal-bipyramidal structure bearing the oxo-ligand. The spin density value decreased from 3.14 to 2.33 a.u. in $\mathbf{6_{6/2}} \rightarrow \mathbf{7_{6/2}}$ (Table S3, ESI†). Then oxidized $\mathbf{7_{6/2}}$ species underwent a strongly exothermic (ΔE = −165 kJ mol^{-1}) hydrolysis step. The Mn center adopted the octahedral coordination in the $\mathbf{8_{6/2}}$ intermediate formed upon the hydrolysis.

The structural flexibility of the unconstrained cluster model provides sufficient space for the relaxation upon the interaction with the oxidative species needed to ensure the overall stability of the extended periodic structure composed of such units. Here we infer that the potential degradation paths are initiated when the ROS binding induces severe structural deformations that substantially alter the coordination polyhedra of the Mn sites. Although the introduction of the hard geometric constraints decreased the exothermicity of the formation of the adsorption complexes (Fig. S1 and Table S1, ESI†), the effects were minor and did not affect the main conclusions made on the basis of the fully relaxed models that have been discussed above. In some cases, we, however, observed the enhancement of the reactivity of the Mn sites owing to the excessive strain provided by the constrained benzoate ligands, which resulted in some cases in decoordination events and structural alteration of the otherwise stable geometries (Fig. S2, ESI†). These effects appear to be highly model-dependent and are not expected to be representative to the sufficiently flexible MOF structures that are captured by the relaxed cluster models.

4. Conclusions

Density functional theory calculations have been performed to investigate the interactions of common oxidants (O_2 and H_2O_2) with a cluster model representing the key structural fragment of Mn-BTC MOF. The modeling was performed to assess potential material degradation paths under the oxidizing conditions commonly encountered in pathogenic tissues of living organisms. Such an environment-induced degradation of the nanoporous material was discussed in the context of the development of new approaches for targeted drug delivery.

The calculations indicated the sufficient stability of the Mn-carboxylate structure-forming units towards direct hydrolysis while the interaction with the O_2 and H_2O_2 species led to a facile oxidation of the Mn(2+) to the more thermodynamically stable Mn(4+) state. The oxidation was proceeded with a substantial deformation of the coordination sphere of the transition metal centers and, accordingly, facilitation of the subsequent hydrolysis of the coordination bonds.

DFT calculations showed a facile exchange of non-covalently bound H_2O ligands at the Mn(2+) centers in the Mn-BTC with molecular O_2 resulting in covalent σ, π, or δ bonding. The latter path was more favorable and it resulted in the oxidation of the

Mn center to the formal (4+) state and the formation of a peroxide adduct. The formation of the Mn(3+) state was the result of the O_2 ligand complexation in the σ bonding mode and was likely the intermediate state in the formation of the more stable Mn(4+) counterpart.

On the contrary, hydrogen peroxide molecules bind weakly to the Mn sites. The respective ligand exchange reaction with the starting aqua complex was an exothermic process for the high-lying spin state. The H_2O_2-induced degradation of Mn-BTC in aqueous media involved the cleavage of the O–O bond in the coordinated H_2O_2 molecules, resulting in the oxidation of the Mn(2+) center to the (4+) state, which strongly facilitated the subsequent hydrolysis. Importantly, we note the importance of spin transitions for all reaction paths considered in this study. This has to be properly accounted for in further studies on the stability of Mn-based MOF materials. Our current results clearly show the limited potential of Mn-carboxylate building blocks for oxidation catalysis or gas-sorption applications where the interactions with potential ROS species will inevitably result in the structural distortion of the framework and the long-term degradation of the functional materials. Nevertheless, the favorable reaction paths identified here may be utilized for engineering a new mechanism of the structural response of Mn-containing nanocontainers to pathology-induced alterations of biological environments.

Conflicts of interest

There are no conflicts to declare.

Acknowledgements

This work was supported by the Ministry of Education and Science of the Russian Federation (Project 11.1706.2017/4.6). E. A. P. acknowledges partial support from the European Research Council (ERC) under the European Union's Horizon 2020 research and innovation programme (grant agreement No. 725686). A. V. V. acknowledges the support from the Government of the Russian Federation (Grant 08-08). The Netherlands Organization for Scientific Research (NWO) is acknowledged for providing access to the supercomputer facilities.

References

1 P. W. Siu, J. P. Siegfried, M. H. Weston, P. E. Fuller, W. Morris, C. R. Murdock, W. J. Hoover, R. K. Richardson, S. Rodriguez and O. K. Farha, Boron Trifluoride Gas Adsorption in Metal-Organic Frameworks, *Inorg. Chem.*, 2016, **55**, 12110–12113.
2 T. Simon-Yarza, S. Rojas, P. Horcajada and C. Serre, *The Situation of Metal-Organic Frameworks in Biomedicine*, Elsevier, 2017.
3 J. S. Choi, W. J. Son, J. Kim and W. S. Ahn, *Microporous Mesoporous Mater.*, 2008, **116**, 727–731.
4 N. Wei, Y. Zhang, L. Liu, Z. B. Han and D. Q. Yuan, Pentanuclear Yb(III) cluster-based metal-organic frameworks as heterogeneous catalysts for CO_2 conversion, *Appl. Catal., B*, 2017, **219**, 603–610.
5 T. Rodenas, I. Luz, G. Prieto, B. Seoane, H. Miro, A. Corma, F. Kapteijn, F. X. Llabrés, I. Xamena and J. Gascon, Metal-organic framework nanosheets in polymer composite materials for gas separation, *Nat. Mater.*, 2015, **14**, 48–55.
6 Z.-G. Gu, S. Grosjean, S. Bräse, C. Wöll and L. Heinke, Enantioselective adsorption in homochiral metal–organic frameworks: the pore size influence, *Chem. Commun.*, 2015, **51**, 8998–9001.
7 L. R. Mingabudinova, V. V. Vinogradov, V. A. Milichko, E. Hey-Hawkins and A. V. Vinogradov, Metal–organic frameworks as competitive materials for non-linear optics, *Chem. Soc. Rev.*, 2016, **45**, 5408–5431.
8 Y.-B. Huang, J. Liang, X.-S. Wang and R. Cao, Multifunctional metal–organic framework catalysts: synergistic catalysis and tandem reactions, *Chem. Soc. Rev.*, 2017, **46**, 126–157.
9 L. Zhu, X. Q. Liu, H. L. Jiang and L. B. Sun, *Chem. Rev.*, 2017, **117**, 8129–8176.
10 D. Damasceno Borges, G. Maurin and D. S. Galvão, Design of Porous Metal-Organic Frameworks for Adsorption Driven Thermal Batteries, *MRS Adv.*, 2017, **2**, 519–524.
11 J. J. Low, A. I. Benin, P. Jakubczak, J. F. Abrahamian, S. A. Faheem and R. R. Willis, Virtual high throughput screening confirmed experimentally: Porous coordination polymer hydration, *J. Am. Chem. Soc.*, 2009, **131**, 15834–15842.
12 I. J. Kang, N. A. Khan, E. Haque and S. H. Jhung, Chemical and thermal stability of isotypic metal-organic frameworks: Effect of metal ions, *Chem. – Eur. J.*, 2011, **17**, 6437–6442.
13 C. Y. Sun, C. Qin, C. G. Wang, Z. M. Su, S. Wang, X. L. Wang, G. S. Yang, K. Z. Shao, Y. Q. Lan and E. B. Wang, Chiral nanoporous metal-organic frameworks with high porosity as materials for drug delivery, *Adv. Mater.*, 2011, **23**, 5629–5632.
14 A. C. McKinlay, R. E. Morris, P. Horcajada, G. Férey, R. Gref, P. Couvreur and C. Serre, *Angew. Chem., Int. Ed.*, 2010, **49**, 6260–6266.
15 M. Giménez-Marqués, T. Hidalgo, C. Serre and P. Horcajada, *Coord. Chem. Rev.*, 2016, **307**, 342–360.
16 E. Bellido, M. Guillevic, T. Hidalgo, M. J. Santander-Ortega, C. Serre and P. Horcajada, Understanding the colloidal stability of the mesoporous MIL-100(Fe) nanoparticles in physiological media, *Langmuir*, 2014, **30**, 5911–5920.
17 K. M. L. Taylor-Pashow, J. Della Rocca, Z. Xie, S. Tran and W. Lin, Postsynthetic modifications of iron-carboxylate nanoscale metal-organic frameworks for imaging and drug delivery, *J. Am. Chem. Soc.*, 2009, **131**, 14261–14263.
18 J. Della Rocca, D. Liu and W. Lin, Nanoscale metal-organic frameworks for biomedical imaging and drug delivery, *Acc. Chem. Res.*, 2011, **44**, 957–968.
19 R. Ananthoji, J. F. Eubank, F. Nouar, H. Mouttaki, M. Eddaoudi and J. P. Harmon, Symbiosis of zeolite-like metal–organic frameworks (rho-ZMOF) and hydrogels: Composites for controlled drug release, *J. Mater. Chem.*, 2011, **21**, 9587.
20 P. Horcajada, T. Chalati, C. Serre, B. Gillet, C. Sebrie, T. Baati, J. F. Eubank, D. Heurtaux, P. Clayette, C. Kreuz, J. S. Chang, Y. K. Hwang, V. Marsaud, P. N. Bories, L. Cynober, S. Gil,

G. Férey, P. Couvreur and R. Gref, Porous metal-organic-framework nanoscale carriers as a potential platform for drug delivery and imaging, *Nat. Mater.*, 2010, **9**, 172–178.

21 C.-Y. Sun, C. Qin, X.-L. Wang and Z.-M. Su, Metal-organic frameworks as potential drug delivery systems, *Expert Opin. Drug Delivery*, 2013, **10**, 89–101.

22 S. Fu, C. Zhu, J. Song, D. Du and Y. Lin, *Adv. Energy Mater.*, 2017, 7.

23 P. Canepa, K. Tan, Y. Du, H. Lu, Y. J. Chabal and T. Thonhauser, Structural, elastic, thermal, and electronic responses of small-molecule-loaded metal–organic framework materials, *J. Mater. Chem. A*, 2015, **3**, 986–995.

24 J. a Kellum, M. Song and J. Li, Science review: extracellular acidosis and the immune response: clinical and physiologic implications, *Crit. Care*, 2004, **8**, 331–336.

25 P. J. Barnes, *Free Radical Biol. Med.*, 1990, **9**, 235–243.

26 M. Mittal, M. R. Siddiqui, K. Tran, S. P. Reddy and A. B. Malik, Reactive Oxygen Species in Inflammation and Tissue Injury, *Antioxid. Redox Signaling*, 2014, **20**, 1126–1167.

27 P. Horcajada, C. Serre, G. Maurin, N. A. Ramsahye, F. Balas, M. Vallet-Regí, M. Sebban, F. Taulelle and G. Férey, Flexible porous metal-organic frameworks for a controlled drug delivery, *J. Am. Chem. Soc.*, 2008, **130**, 6774–6780.

28 K. S. Egorova and V. P. Ananikov, Toxicity of Metal Compounds: Knowledge and Myths, *Organometallics*, 2017, **36**, 4071–4090.

29 G. C. Dismukes, Manganese Enzymes with Binuclear Active Sites, *Chem. Rev.*, 1996, **96**, 2909–2926.

30 N. A. Law, M. T. Caudle and V. L. Pecoraro, Manganese Redox Enzymes and Model Systems: Properties, Structures, and Reactivity, *Adv. Inorg. Chem.*, 1998, **46**, 305–440.

31 G. D. Lawrence and D. T. Sawyer, The chemistry of biological manganese, *Coord. Chem. Rev.*, 1978, **27**, 173–193.

32 T. Ladrak, S. Smulders, O. Roubeau, S. J. Teat, P. Gamez and J. Reedijk, Manganese-based metal-organic frameworks as heterogeneous catalysts for the cyanosilylation of acetaldehyde, *Eur. J. Inorg. Chem.*, 2010, 3804–3812.

33 Q. Sun, M. Liu, K. Li, Y. Han, Y. Zuo, F. Chai, C. Song, G. Zhang and X. Guo, Synthesis of Fe/M (M = Mn, Co, Ni) bimetallic metal organic frameworks and their catalytic activity for phenol degradation under mild conditions, *Inorg. Chem. Front.*, 2017, **4**, 144–153.

34 C. Pereira, M. Simoes, J. Tome and F. Almeida Paz, Porphyrin-Based Metal-Organic Frameworks as Heterogeneous Catalysts in Oxidation Reactions, *Molecules*, 2016, **21**, 1348.

35 Y. Ming, J. Purewal, J. Yang, C. Xu, R. Soltis, J. Warner, M. Veenstra, M. Gaab, U. Müller and D. J. Siegel, Kinetic stability of MOF-5 in humid environments: Impact of powder densification, humidity level, and exposure time, *Langmuir*, 2015, **31**, 4988–4995.

36 P. Guo, D. Dutta, A. G. Wong-Foy, D. W. Gidley and A. J. Matzger, *J. Am. Chem. Soc.*, 2015, **137**, 2651–2657.

37 A. Dhakshinamoorthy, M. Alvaro and H. Garcia, Metal–organic frameworks as heterogeneous catalysts for oxidation reactions, *Catal. Sci. Technol.*, 2011, **1**, 856.

38 S. Zuluaga, E. M. A. Fuentes-Fernandez, K. Tan, F. Xu, J. Li, Y. J. Chabal and T. Thonhauser, Understanding and controlling water stability of MOF-74, *J. Mater. Chem. A*, 2016, **4**, 5176–5183.

39 D. Wu, W. Yan, H. Xu, E. Zhang and Q. Li, Defect engineering of Mn-based MOFs with rod-shaped building units by organic linker fragmentation, *Inorg. Chim. Acta*, 2017, **460**, 93–98.

40 Y. Kuwahara, Y. Yoshimura and H. Yamashita, Liquid-phase oxidation of alkylaromatics to aromatic ketones with molecular oxygen over a Mn-based metal–organic framework, *Dalton Trans.*, 2017, **46**, 8415–8421.

41 R. E. Hansen and S. Das, Biomimetic di-manganese catalyst cage-isolated in a MOF: robust catalyst for water oxidation with Ce^{iv}, a non-O-donating oxidant, *Energy Environ. Sci.*, 2014, **7**, 317–322.

42 D. H. Lee, S. Kim, M. Y. Hyun, J.-Y. Hong, S. Huh, C. Kim and S. J. Lee, Controlled growth of narrowly dispersed nanosize hexagonal MOF rods from Mn(III)–porphyrin and $In(NO_3)_3$ and their application in olefin oxidation, *Chem. Commun.*, 2012, **48**, 5512.

43 S. Bhattacharjee, D.-A. Yang and W.-S. Ahn, A new heterogeneous catalyst for epoxidation of alkenes via one-step post-functionalization of IRMOF-3 with a manganese(ii) acetylacetonate complex, *Chem. Commun.*, 2011, **47**, 3637.

44 J. Ye and C. Liu, $Cu_3(BTC)_2$: CO oxidation over MOF based catalysts, *Chem. Commun.*, 2011, **47**, 2167.

45 K. Brown, S. Zolezzi, P. Aguirre, D. Venegas-Yazigi, V. Paredes-García, R. Baggio, M. A. Novak and E. Spodine, $[Cu(H_2btec)(bipy)]_\infty$: a novel metal organic framework (MOF) as heterogeneous catalyst for the oxidation of olefins, *Dalton Trans.*, 2009, 1422.

46 K. K. Tanabe and S. M. Cohen, Engineering a metal-organic framework catalyst by using postsynthetic modification, *Angew. Chem., Int. Ed.*, 2009, **48**, 7424–7427.

47 M. Zhang, X. Huang and Y. Chen, DFT insights into the adsorption of NH_3-SCR related small gases in Mn-MOF-74, *Phys. Chem. Chem. Phys.*, 2016, **18**, 28854–28863.

48 P. Maitarad, S. Namuangruk, D. Zhang, L. Shi, H. Li, L. Huang, B. Boekfa and M. Ehara, Metal-porphyrin: A potential catalyst for direct decomposition of N_2O by theoretical reaction mechanism investigation, *Environ. Sci. Technol.*, 2014, **48**, 7101–7110.

49 P. Maitarad, J. Meeprasert, L. Shi, J. Limtrakul, D. Zhang and S. Namuangruk, Mechanistic insight into the selective catalytic reduction of NO by NH_3 over low-valent titanium-porphyrin: A DFT study, *Catal. Sci. Technol.*, 2016, **6**, 3878–3885.

50 M. J. Frisch *et al.*, *Gaussian 09, Revis. D.01*, 2009.

51 V. V. Vinogradov, A. S. Drozdov, L. Mingabudinova, E. M. Shabanova, N. Kolchina, E. I. Anastasova, A. A. Markova, A. Shtil, V. Milichko, G. L. Starova, R. Precker, A. Vinogradov, E. Hey-Hawkins and E. Pidko, Composites Based on Heparin and MIL-101(Fe): The Drug Releasing Depot for Anticoagulant Therapy and Advanced Medical Nanofabrication, *J. Mater. Chem. B*, 2018, **6**, 2450–2459.

52 J. P. Perdew, K. Burke and M. Ernzerhof, Generalized Gradient Approximation Made Simple, *Phys. Rev. Lett.*, 1996, **77**, 3865–3868.

53 S. Grimme, J. Antony, S. Ehrlich and H. Krieg, A consistent and accurate ab initio parametrization of density functional dispersion correction (DFT-D) for the 94 elements H-Pu, *J. Chem. Phys.*, 2010, **132**, 154104.
54 S. Grimme, Semiempirical GGA-type density functional constructed with a long-range dispersion correction, *J. Comput. Chem.*, 2006, **27**, 1787–1799.
55 S. Miertuš, E. Scrocco and J. Tomasi, Electrostatic interaction of a solute with a continuum. A direct utilization of ab initio molecular potentials for the prevision of solvent effects, *Chem. Phys.*, 1981, **55**, 117–129.
56 E. Stavitski, E. A. Pidko, S. Couck, T. Remy, E. J. M. Hensen, B. M. Weckhuysen, J. Denayer, J. Gascon and F. Kapteijn, Complexity behind CO_2 capture on NH_2-MIL-53(Al), *Langmuir*, 2011, **27**, 3970–3976.
57 J. Van Den Bergh, C. Gücüyener, E. A. Pidko, E. J. M. Hensen, J. Gascon and F. Kapteijn, Understanding the anomalous alkane selectivity of ZIF-7 in the separation of light alkane/alkene mixtures, *Chem. – Eur. J.*, 2011, **17**, 8832–8840.
58 Chemcraft, http://www.chemcraftprog.com, accessed 5 January 2018.
59 L. R. Falvello, B. M. Foxman and C. A. Murillo, Fitting the Pieces of the Puzzle: The δ Bond, *Inorg. Chem.*, 2014, **53**, 9441–9456.
60 C. E. Housecroft and A. G. Sharpe, *Inorganic Chemistry*, Pearson Education Limited, Harlow, 4th edn, 2012.